DOI: 10.61782/fa.2023.0763

forum acusticum 2023

A HYBRID NUMERICAL APPROACH TO QUANTIFY DIRECTIVITY PATTERNS USING PHASELESS HYDROACOUSTIC DATA

Andrés Prieto[1*] **Sara Recondo**[2]
[1] Galician Center for Mathematical Research and Technology, University of A Coruña, Spain
[2] Marine Instruments, University of A Coruña, Spain

ABSTRACT

Hydroacoustic transducers have been used profusely in monitoring activities in coastal and oceanic marine environments for fishery purposes and the health evaluation of the seabed and its related biological ecosystems. Accurately predicting its directivity patterns plays a crucial role in the subsequent numerical simulations of complex marine environments. The transducers can be quickly characterized experimentally using in-house laboratory equipment where their acoustic response can be obtained from time-harmonic near-field phaseless data. Obviously, the extrapolation of those near-field data to predict the time-harmonic far-field generated pressure cannot be computed straightforwardly and requires estimating the directivity pattern associated with the transducer. A hybrid approach based on the combination of data-driven reconstruction techniques and an integral representation of the pressure field is analyzed in this work. The accuracy of the proposed methodology is illustrated in realistic scenarios with available closed-form solutions such as omnidirectional sources and end-fire arrays. The impact of using different phase retrieval and quadrature methods is also quantified numerically.

Keywords: *Hydroacoustics, directivity, integral methods, phaseless data.*

1. INTRODUCTION

One of the most widely used indirect procedures to detect fish schools and estimate their biomass in underwater environments consists of the measure of the volume backscattering strength of the reflected pressure field generated by a hydroacoustic transducer. The transducer insonifies the water column, and reflected echoes coming from fish schools or the vegetation on the seabed, are backpropagated to the sea surface and recorded by the transducer. The strength of the reflected signal is used to estimate the density and biomass of the fish schools [1,2].

Hydroacoustic transducers must be calibrated to ensure accurate pressure field predictions. This calibration process involves characterizing the directivity pattern of the hydroacoustic transducer from near-field pressure measurements [3]. The directivity pattern describes how efficiently the transducer emits acoustic energy in different spatial directions. This information is crucial for accurately reading the reflected signal recorded by the hydroacoustic transducer. Directivity patterns can be measured in a controlled environment such as a laboratory test tank, where free-field conditions can be reproduced [4]. The present work is focused on the characterization of the directivity pattern of a hydroacoustic transducer when only partial (phaseless) information of the free-field pressure field is available in the calibration process.

2. MODELLING NEAR-FIELD PRESSURE GENERATED BY A TRANSDUCER

The mathematical modelling assumptions in underwater acoustics can be grouped in two different environments regarding the distance to the origin of the acoustic source: Far-field data means measurements far from the transducer at a distance $r \gg \lambda = c/f$ (in seawater at 50kHz: $\lambda \simeq 3$cm) or near-field data means measurements close to the transducer at a distance $r \equiv \lambda$.

In the present work, the calibration measurements of the acoustic transducer have been made at in-house facil-

*__Corresponding author__: andres.prieto@udc.es.

ities: $r \simeq 10\lambda$ implies near-field data. In addition, the typical size of the active surface of the acoustic transducer is much smaller than r, which enables us to consider the following simplification: the acoustic source can be considered with pointwise support.

In this simple scenario, classical integral methods (see, e.g. [5]) allow recovering time-harmonic far-field pressure fields generated from a pointwise-support axis-symmetric source at a fixed frequency value. If the compressible fluid is assumed dissipative (which is the case for seawater at the middle and high-frequency regimes), the pressure field is given by

$$p(x,y,z) = \mathrm{i}k(\omega) \int_0^{\pi/2-i\infty} J_0\left(k(\omega)R(x,y)\sin\left(\theta\right)\right) \times e^{-\mathrm{i}k(\omega)z\cos\left(\theta\right)} \hat{S}(\theta)\sin(\theta)\,\mathrm{d}\theta, \quad (1)$$

where ω is the angular frequency, $k(\omega) = \omega/c + \mathrm{i}\alpha\omega^2$ is the wavenumber, c is the sound speed, α is the volume dissipation coefficient, J_0 is the 0-th order first-kind Bessel function, $\hat{S}(\theta)$ is the directivity pattern, $R(x,y) = \sqrt{x^2+y^2}$, and the real-valued instances of θ represent the azimuth angle in cylindrical coordinates. In what follows, the reference values for the seawater in the near-field measurements predicted in the numerical simulations are given by $\omega = 100\pi$ rad/s, $\alpha = 6.4 \times 10^{-16}$ s, $c = 1430$ m/s. The pressure field will be measured at a constant depth $z = -0.3$ m.

Through the rest of this work, the numerical illustrations are made using a directivity pattern generated by a parametric end-fire array [6], whose function $S(\theta)$ can be computed in closed-form, given by

$$\hat{S}(\theta) = Q\frac{1-e^{-\mathrm{i}k(\omega)L(1-\cos\theta)}}{\mathrm{i}k(\omega)(1-\cos\theta)},$$

where Q is the volume strength of the source and L is the array length.

3. NUMERICAL EVALUATION OF THE INTEGRAL REPRESENTATION

The direct numerical evaluation of the integral (1) requires of a straightforward change of variable to avoid computational over floating computations:

$$p(x,y,z) = \mathrm{i}k(\omega)\int_0^1 J_0\left(k(\omega)R(x,y)\sqrt{1-u^2}\right)e^{-\mathrm{i}k(\omega)zu}S(u)\,\mathrm{d}u - k(\omega)\int_0^\infty J_0\left(k(\omega)R(x,y)\sqrt{1+t^2}\right)e^{k(\omega)zt}S(it)\,\mathrm{d}t, \quad (2)$$

with $u = \cos\theta$ for $\theta \in [0,\pi/2]$ and $t = -\mathrm{i}\cos\theta$ for $\theta \in [\pi/2, \pi/2 - \mathrm{i}\infty)$.

In the case of the numerical quadrature in the real path, $u \in [0,1]$, different numerical rules can be used, such as composite trapezoidal rule, Clenshaw-Curtis quadrature, Gauss-Legendre quadrature, or Gauss-Patterson nested rules. In the case of the numerical quadrature in the imaginary path, $t \in [0,\infty)$, the Gauss-Laguerre quadrature or the above-mentioned rules but applied in a truncated interval $[0,T]$ with $T = 30/(zk(\omega))$. These quadrature procedures have been tested in two simple scenarios where an analytical closed-form solution is available for the computation of the integral value. In the case of the real path, the value of

$$\int_0^1 J_1(k(\omega)R(x,y)\sqrt{1-u^2})\,\mathrm{d}u, \quad (3)$$

has been computed. In the case of the complex path, the integral

$$k(\omega)\int_0^\infty J_0(k(\omega)R(x,y)t)e^{k(\omega)zt}\,\mathrm{d}t, \quad (4)$$

has been used for testing the quadrature rules. The relative errors of both real- and imaginary paths are shown in Figures 1 and 2, respectively. Due to the performance of the different quadrature rules, in what follows, the Gauss-Patterson nested rule will be used with order 511 (which corresponds to the 8th nested index [7]).

4. DISCRETIZATION OF THE NEAR-FIELD INTEGRAL OPERATOR WITH FULL DATA

The inversion problem consists in how to compute the values of the directivity pattern in terms of the pressure field measurements. It requires a discretization of the directivity profile $S(\theta)$. With this purpose, two different alternatives are presented: a classical piecewise linear finite element interpolation and a novel enriched strategy based on the Partition of Unity Finite Element Method (PUFEM) introduced by Melenk and Babuska [8].

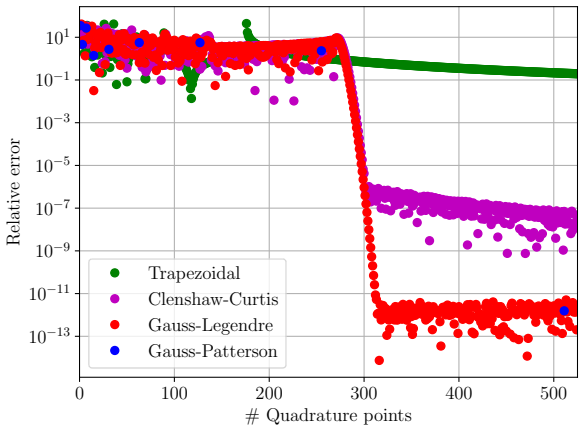

Figure 1. Relative error of the quadrature rule in (3) plotted with respect to the number of nodes.

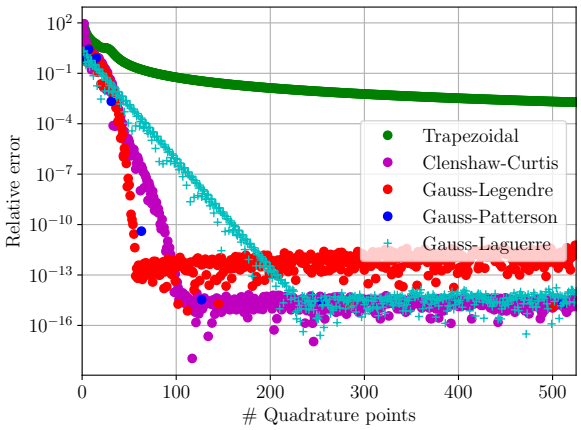

Figure 2. Relative error of the quadrature in (4) rule plotted with respect to the number of nodes.

4.1 Finite element (FEM) discretization

The FEM discretization of the directivity pattern is computed on an equispaced mesh $\mathcal{T}_h$ in the complex-valued integral path with $N = N_{\text{re}} + N_{\text{im}}$ vertices:

$$u_1, \dots, u_{N_{\text{re}}} \in [0, 1],$$
$$\text{i}t_{N_{\text{re}}+1}, \dots, \text{i}t_{N_{\text{re}}+N_{\text{im}}} \in [0, iT].$$

Then a piecewise linear FEM approximation of $S(u)$ in $V_h = \langle \{\phi_n\}_{n=1}^N \rangle$ is defined

$$S(u) \approx S_h(u) = \sum_{n=1}^{N} S_n \phi_n(u),$$

where $\phi_n|_T \in \mathbb{P}_1(\mathbb{C})$, $T \in \mathcal{T}_h$. Consequently, the FEM discretization of pressure at measurement points $1 \le m \le M$ are computed as follows

$$p(x_m, y_m, z_m) = \sum_{n=1}^{N} S_n k(\omega) \Bigg(\text{i} \int_0^1 J_0(k(\omega) R(x,y) \sqrt{1-u^2}) e^{-ik(\omega)zu} \phi_n(u)\, \mathrm{d}u - \int_0^T J_0(k(\omega) R(x,y) \sqrt{1+t^2}) e^{-k(\omega)zu} \phi_n(it)\, \mathrm{d}t \Bigg). \tag{5}$$

Hence, in this FEM discretization setting, the inverse problem with full data (including amplitude and phase in the pressure measurements) can be written as follows: Given $\vec{b} \in \mathbb{C}^M$ the measurements vector, find $\vec{S}_h \in \mathbb{C}^N$ such that

$$\mathcal{A}\vec{S}_h = \vec{b}, \qquad \mathcal{A} \in \mathcal{M}_{M\times N}(\mathbb{C}), \quad M > N, \tag{6}$$

where the matrix coefficients $\mathcal{A}_{nm}$ are given by the right-hand side in (5) and the vector components b_m are the pressure values of the left-hand side in (5). The solution of the inverse problem (6) has been computed using a least-square procedure. The numerical results are shown in Figures 3 and 4. Since the matrix $\mathcal{A}$ is ill-conditioned, spurious oscillations arise in the prediction of the directivity pattern. Moreover, the numerical solution is completely polluted if $\text{dist}(S_{\text{ex}}, V_h)$ is not small enough. These inaccuracies cannot be solved by refining the mesh since the number of measurement points (which is fixed by the experiment design) cannot be smaller than the dimension of the FEM discrete space. Hence, the condition $M > N$ is a requirement in the inverse problem. Hence, potential standard remedies such as h-refinement or p-refinement are not allowed.

4.2 Partition of Unity Finite element (PUFEM) discretization

Taking into account that the FEM basis $\{\phi_n\}_{n=1}^N$ are a partition of unity (i.e. $\sum_{n=1}^N \phi_n = 1$), the piecewise polynomial discrete space $V_h = \langle \{\phi_n\}_{n=1}^N \rangle$ is enriched with wave-like functions (see [8] for further details)

$$w_j(u) = \frac{1 - e^{\text{i}k(\omega)L_j}}{u}, \quad L_j > 0, \quad 1 \le j \le J.$$

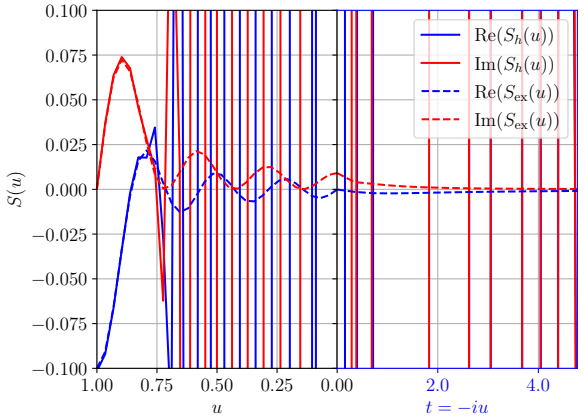

Figure 3. Directivity pattern computed solving the inverse problem with full data using a FEM discretization, plotted in the real and imaginary path.

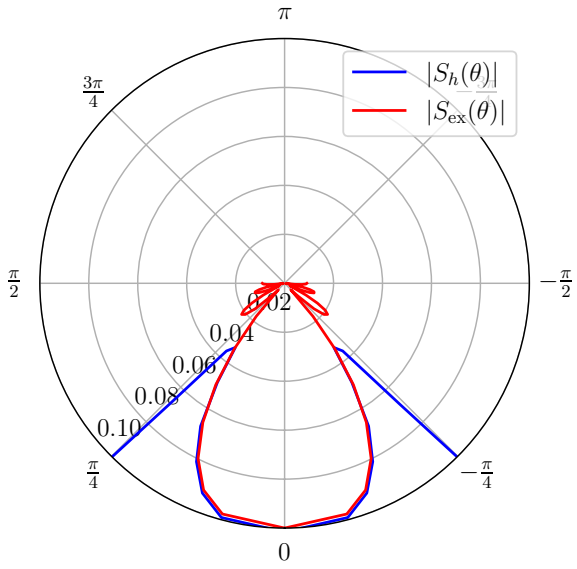

Figure 4. Polar plot of directivity pattern computed solving the inverse problem with full data using a FEM discretization.

Hence, the PUFEM discrete space is defined by $V_h = \langle \{w_j \phi_n\}_{j,n=1}^{J,N} \rangle$. Then a PUFEM approximation of $S(u)$ belonging to V_h is defined

$$S(u) \approx S_h(u) = \sum_{j=1}^{J} \sum_{n=1}^{N} S_n w_j(u) \phi_n(u),$$

where $\phi_n|_T \in \mathbb{P}_1(\mathbb{C})$, $T \in \mathcal{T}_h$. In this manner, the PUFEM discretization of pressure at measurement points $1 \leq m \leq M$ are computed as follows

$$p(x_m, y_m, z_m) = \sum_{j=1}^{J} \sum_{n=1}^{N} S_n k(\omega) \Bigg(\mathrm{i} \int_0^1 J_0(k(\omega) R(x,y) \sqrt{1-u^2}) e^{-\mathrm{i} k(\omega) z u} w_j(u) \phi_n(u) \, \mathrm{d}u - \int_0^T J_0(k(\omega) R(x,y) \sqrt{1+t^2}) e^{-k(\omega) z u} w_j(\mathrm{i}t) \phi_n(\mathrm{i}t) \, \mathrm{d}t \Bigg). \tag{7}$$

The PUFEM discretization leads to an analogous rewriting of the inverse problem with full data (including amplitude and phase in the pressure measurements) as follows: Given $\vec{b} \in \mathbb{C}^M$ the measurements vector, find $\vec{S}_h \in \mathbb{C}^{JN}$ such that

$$\vec{S}_h = \underset{\vec{S} \in \mathbb{C}^{JN}}{\arg\min} ||\mathcal{A}\vec{S} - \vec{b}||, \tag{8}$$

where $\mathcal{A} \in \mathcal{M}_{M \times JN}(\mathbb{C})$ and it is required $M \geq JN$. Notice that the matrix coefficients $\mathcal{A}_{nm}$ are given by the right-hand side in (7) and the vector components b_m are the pressure values of the left-hand side in (7). The solution of the inverse problem (8) has been computed using a least-square procedure. The numerical results are shown in Figures 5 and 6. Once the discrete space has been enriched with wave-like functions (in this case, only with one enriched function), the directivity pattern is recovered accurately by using the full data for the pressure measurements.

5. PHASE-RETRIEVAL STRATEGIES APPLIED TO THE DIRECTIVITY PATTERN FOR PHASELESS DATA

If the full information of the pressure measurements is not available, i.e., the phase of those pressure values is not recorded, the inverse problem to characterize the directivity pattern of the transducer becomes a non-linear problem: Given $\vec{b} \in \mathbb{R}^{+M}$ the measurements vector, find $\vec{S}_h \in \mathbb{C}^{JN}$ such that

$$|\mathcal{A}\vec{S}_h| = \vec{b}, \quad \mathcal{A} \in \mathcal{M}_{M \times JN}(\mathbb{C}), \quad M \geq 2JN. \tag{9}$$

In the present work, three different strategies are used based on three different kinds of phase retrieval approaches. First, the fixed-point approach is considered by

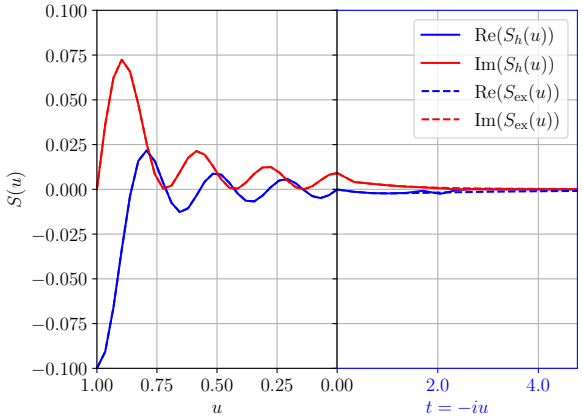

Figure 5. Directivity pattern computed solving the inverse problem with full data using a PUFEM discretization, plotted in the real and imaginary path.

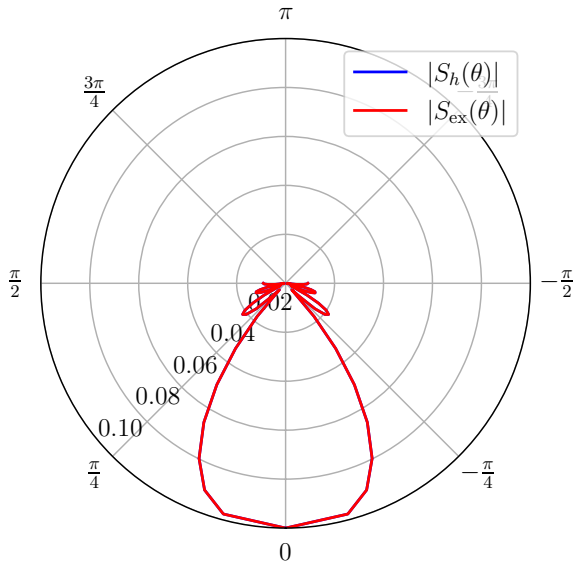

Figure 6. Polar plot of directivity pattern computed solving the inverse problem with full data using a PUFEM discretization.

using the alternating projection (AP) method [9]. Then, the feasibility approach has been implemented by means of the averaged alternating reflections (AAR) method [10]. Finally, the phase retrieval problem is solved using non-convex optimization and, in particular, solved using the non-linear least-square (LS) method [11].

5.1 Fixed point approach

The alternating projection (AP) method is one of the classical fixed point approaches to solving the non-linear inverse problem (9): Given $\vec{b} \in \mathbb{R}^{+M}$ the measurements vector, from an initial guess $\vec{S}_h^0$, compute $\vec{S}_h^{k+1}$ such that

$$\vec{S}_h^{k+1} = \mathcal{A}^*(\vec{b} \odot \text{phase}(\mathcal{A}\vec{S}_h^k)), \qquad k = 0, \dots, I_{\max},$$

until a tolerance threshold is satisfied or a maximum number of iterations $I_{\max}$ is reached. This AP method requires the Hadarmard product between vectors, denoted by $\odot$ and the computation of the phase of each vector component, which is inexpensive from a computational point of view.

This fixed-point approach requires that matrix $\mathcal{A}$ must be unitary. Due to this restriction, the problem (9) is rewritten using the singular value decomposition (SVD) $\mathcal{A} = \mathcal{U}\Sigma\mathcal{V}^*$ as follows: compute S_h^{k+1} such that

$$\begin{aligned} \vec{y}_h^{k+1} &= \mathcal{U}^*(\vec{b} \odot \text{phase}(\mathcal{U}\vec{y}_h^k)), \\ S_h^{k+1} &= \mathcal{V}\Sigma^{-1}\vec{y}_h^{k+1}, \qquad k = 0, \dots, I_{\max}. \end{aligned}$$

Figure 7 shows the number of iterations required to reach convergence depending on the Signal-to-Noite ratio added in the initial guess used to start the AP iterative procedure. It can be observed that an accurate initialization is required to limit the number of iterations.

5.2 Feasibility approach

The prototypical example of a feasibility approach consists of the classical Averaged Alternating Reflections (AAR). If this method is applied to solve the non-linear inverse problem (9) can be written as follows: Given $\vec{b} \in \mathbb{R}^{+M}$ the measurements vector,

$$\text{Find } \vec{d}_h \in X \cap Y,$$

where $X = \text{range}\,\mathcal{A}$ and $Y = \{\vec{d} \in \mathbb{C}^M : |\vec{d}| = \vec{b}\}$. To compute iteratively a feasible solution to the problem above, successive projections into the linear space X and the set Y must be performed. As in the case of the AP method, this feasibility approach requires that matrix $\mathcal{A}$ must be unitary. Due to this restriction, the problem (9) is rewritten using the SVD decomposition $\mathcal{A} = \mathcal{U}\Sigma\mathcal{V}^*$:

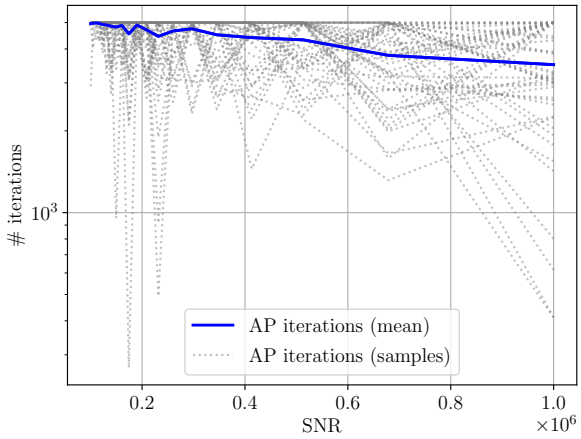

Figure 7. Number of iterations of the AP method with respect to the SNR present in the initial guess of the iterative procedures.

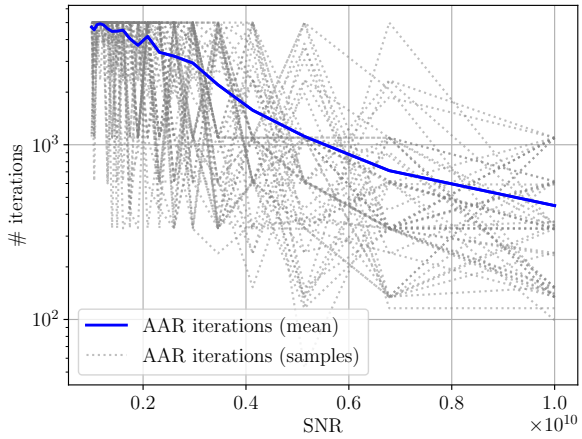

Figure 8. Number of iterations of the AAR method with respect to the SNR present in the initial guess of the iterative procedures.

From an initial guess $\vec{d}_h^{\,0}$, compute S_h^{k+1} such that

$$\vec{d}_h^{\,k+1} = \frac{1}{2}\vec{d}_h^{\,k} + \frac{1}{2}\mathcal{R}_X\mathcal{R}_y\vec{d}_h^{\,k},$$
$$S_h^{k+1} = \mathcal{V}\Sigma^{-1}\mathcal{U}^*\vec{y}_h^{\,k+1}, \qquad k = 0, \ldots, I_{\max},$$

where

$$\mathcal{R}_X\vec{d} = 2\mathcal{U}\mathcal{U}^*\vec{d} - \vec{d},$$
$$\mathcal{R}_Y = 2\vec{b} \odot \text{phase}(\vec{d}) - \vec{d}.$$

Notice that the projections $\mathcal{P}_X$ and $\mathcal{P}_Y$ onto X and Y, respectively, are not written explicitly in the iterative procedure described above. However, they are involved in those computations since $\mathcal{P}_X\vec{d} = \mathcal{U}\mathcal{U}^*\vec{d}$ and $\mathcal{P}_Y\vec{d} = \vec{b} \odot \text{phase}(\vec{d})$.

Figure 8 shows the number of iterations required to reach convergence depending on the Signal-to-Noite ratio added in the initial guess used to start the AP iterative procedure. It can be observed again that an accurate initialization is required to limit the number of iterations.

5.3 Non-convex optimization

Finally, a non-convex optimization point of view can be used to solve the non-linear inverse problem (9). With this goal, a non-linear least squares (LS) has been considered as follows: Given $\vec{b} \in \mathbb{R}^{+M}$ the measurements vector, find $\vec{S}_h \in \mathbb{C}^{JN}$ such that

$$\vec{S}_h = \underset{\vec{S}\in\mathbb{C}^{JN}}{\arg\min} ||\mathcal{A}\vec{S} - \vec{b}||,$$

where $\mathcal{A} \in \mathcal{M}_{M\times JN}(\mathbb{C})$ and $M \geq 2JN$. Despite this approach does not require to work with unitary matrices since $\mathcal{A}$ is very ill-conditioned, the SVD decomposition $\mathcal{A} = \mathcal{U}\Sigma\mathcal{V}^*$ is used to work with well-balanced unitary matrices. In that manner, the LS optimization problem associated with (9) can be stated as follows:

$$\vec{y}_h = \underset{\vec{y}\in\mathbb{C}^{JN}}{\arg\min} ||\mathcal{U}\vec{y} - \vec{b}||,$$
$$S_h = \mathcal{V}\Sigma^{-1}\vec{y}_h.$$

Even in this case, an initial guess is required to solve the LS optimization problem.

Figure 9 shows the number of iterations required to reach convergence depending on the Signal-to-Noite ratio added in the initial guess used to start the LS optimization procedure. It can be observed again that an accurate initialization is required to limit the number of iterations. However, this LS optimization procedure exhibits a more robust behaviour with larger values of SNR in the initial guess, and it requires less number of iterations than the AP and AAR approaches.

6. CONCLUSIONS

The present contribution models the near-field of an underwater transducer by means of an integral representation used for the pressure field generated by an acoustic pointwise source. The nested Gauss-Patterson quadrature

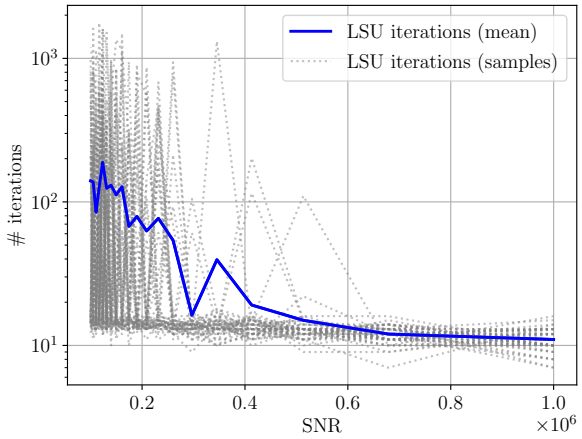

Figure 9. Number of iterations of the LS method with respect to the SNR present in the initial guess of the iterative procedures.

is used to evaluate both real and imaginary path integrals. Instead of using a standard linear pointwise approximation, a novel PUFEM method is used to approximate the directivity pattern. The use of this discretization leads to accurate results when the full data is available. Otherwise, the numerical solution of the phase retrieval inverse problem requires an accurate initialization is required to limit the number of iterations required for convergence.

7. ACKNOWLEDGMENTS

The authors are partially supported by the Industrial Doctorate Programme 19/IN606D/2021/2609949 funded by Xunta de Galicia (GAIN and Consellería de Cultura, Educación e Universidade).

8. REFERENCES

[1] T. K. Stanton, P. H. Wiebe, D. Chu, M. C. Benfield, L. Scanlon, L. Martin, and R. L. Eastwood, "On acoustic estimates of zooplankton biomass," *ICES Journal of Marine Science*, vol. 51, no. 4, pp. 505–512, 1994.

[2] D. Li, Y. Hao, and Y. Duan, "Nonintrusive methods for biomass estimation in aquaculture with emphasis on fish: a review," *Reviews in Aquaculture*, vol. 12, no. 3, pp. 1390–1411, 2020.

[3] C. H. Sherman and J. L. Butler, *Transducers and arrays for underwater sound*, vol. 4. Springer, 2007.

[4] I. Sil'vestrov, "Measurement of the sensitivity and directivity pattern of hydroacoustic measuring modules in artificial tanks," *Measurement Techniques*, vol. 49, pp. 1059–1063, 2006.

[5] L. Brekhovskikh, *Waves in layered media*, vol. 16. Elsevier, 2012.

[6] V. F. Humphrey, "The measurement of acoustic properties of limited size panels by use of a parametric source," *Journal of sound and vibration*, vol. 98, no. 1, pp. 67–81, 1985.

[7] T. N. Patterson, "The optimum addition of points to quadrature formulae," *Mathematics of Computation*, vol. 22, no. 104, pp. 847–856, 1968.

[8] J. M. Melenk and I. Babuška, "The partition of unity finite element method: basic theory and applications," *Computer methods in applied mechanics and engineering*, vol. 139, no. 1-4, pp. 289–314, 1996.

[9] R. W. Gerchberg, "A practical algorithm for the determination of plane from image and diffraction pictures," *Optik*, vol. 35, no. 2, pp. 237–246, 1972.

[10] P. Giselsson and S. Boyd, "Linear convergence and metric selection for douglas-rachford splitting and admm," *IEEE Transactions on Automatic Control*, vol. 62, no. 2, pp. 532–544, 2016.

[11] M. Soltanolkotabi, *Algorithms and theory for clustering and nonconvex quadratic programming*. Stanford University, 2014.